Journal of Materials Chemistry A

Accepted Manuscript

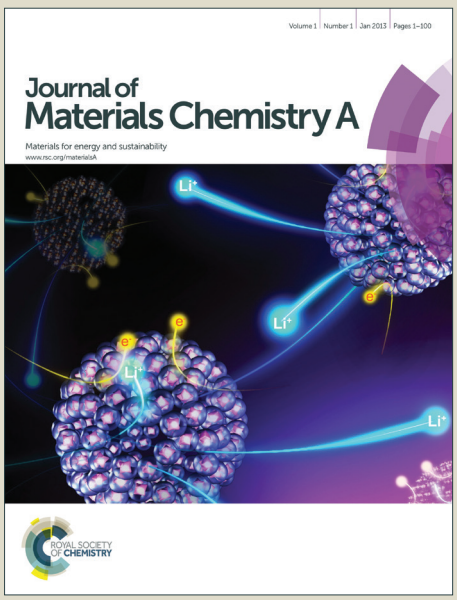

ROYAL SOCIETY OF CHEMISTRY

www.rsc.org/materialsA

Three-dimensional hierarchical nitrogen-doped arch and hollow nanocarbons: Morphological influences in the supercapacitor applications

Prakash Ramakrishnan[a], Soo-Gil Park[b] and Sangaraju Shanmugam[a,*]

[a] Department of Energy Systems Engineering,

Daegu Gyeongbuk Institute of Science & Technology (DGIST), Daegu, 711-873,

Republic of Korea.

*Corresponding author: Tel: +82-53-785-6413. E-mail: sangarajus@dgist.ac.kr

[b] Department of Industrial Engineering Chemistry,

Chungbuk National University, Cheongju 361-763,

Republic of Korea.

Abstract

We report the nitrogen (N) doped nanocarbons with two different morphologies, arch and hollow structure, for supercapacitor (SCs) application. The simple co-axial electrospinning approach, subsequent leaching and carbonization process are employed to fabricate the N-doped carbon nanostructures. The fabricated N-doped arch and hollow nanocarbons exhibit high N-contents of 9.02 and 8.73 wt%; high surface area of 619 and 557 m^2 g^{-1}; total pore volumes of 0.6589 and 0.5681 cm^3 g^{-1}, respectively. The N-doped arch and hollow nanocarbons exhibit the maximum specific capacitances (C_{sp}) of 417 and 371 F g^{-1} at 2 mV s^{-1} in three-electrode system and the C_{sp} of 230 and 212 F g^{-1} at 2 mV s^{-1} for two-electrode system, respectively in 1M H_2SO_4 solution. The maximum energy densities of 8.4 and 7.5 Wh kg^{-1} are obtained for N doped arch and hollow nanocarbons, respectively. Further, these novel carbon nanostructures also deliver good cycle stabilities of 98% for 5000 cycles at a current density of 1 A g^{-1}. Such outstanding SCs electro-sorption ability is due to high micro-texture and high N-content characteristics of carbon nanostructures.

Keywords: Electrospinning; nanocarbons; supercapacitors; nitrogen-doped carbon

1. Introduction

Over the past few decades, great interest has been riveted on porous carbon materials, a class of nanocarbons, in energy storage and conversion devices, and gas sorbent applications owing to their cost-effectiveness, tunable microstructure, at ease of availability and surface functionalization.[1–9] Particularly, the extensive studies have focused on the development of porous carbon with the heteroatoms (B, N, O, P, and S) incorporated into carbon frameworks; the surface

functionalization with heteroatoms enhance the electro-sorption and gas sorption ability.[10–17] Particularly the nitrogen, as the electronegativity of N (3.04) is higher than the carbon atom (2.55). [18] Thus, doping of N-atom could possibly develop a positive charge density along the neighbor carbon atoms. Hence, the electron donor-acceptor characteristics of carbon materials are altered in a positive manner, which results in enhancement of electron donor tendency, electrical conductivity, basicity, adsorption of acidic gases and improves the wettability of carbon in aqueous solution. Such N-functionalised carbon materials have drawn much attention in supercapacitors (SCs), CO_2 capture and electrocatalysis for fuel cell application. [19–22]

Utilization of such material properties have been realized mostly in SCs as an electrode material, which is due to the necessity of highly efficient energy storage for modern society.[23,24]As a result, N-doped porous carbon has been regarded as a potential electrode material for SCs application as it combines the synergistic of pseudo-capacitance, charge storage through Faradic reactions and double layer capacitance, where the charges are accumulated on the electrode surface through non-Faradic phenomenon. Based on this aspect, intense research works have been devoted to prepare the N- doped porous carbon materials.[25]

Generally, N-doped porous carbon materials are prepared by post heat treatment process using high surface area carbon materials under ammonia [26] or urea [27] as an N-source, which results in low N-doping due to the limitation of surface interaction of N precursor on carbon materials, during synthesis process. Besides, using ammonia is harmful to the environment. This approach was then overcome by an in-situ synthesis approach i.e., hard and soft template approach[28–31] ; using expensive sacrificial scaffolds with infiltrating N-doped carbon material as precursor such as acetonitrile,[32] melamine,[33] polypyrrole (PPy),[34] polyaniline (PANi),[35] and polyacrylonitrile (PAN).[36] After carbonization and the removal of template, the N-doped porous carbon structure is

left behind. Thus, a high amount of N content can be preserved by controlling the carbonization temperature, in comparison to the post heat treatment method. Although an *in-situ* approach has been reported successful in preparing high level heteroatom doping in porous carbon material it can be limited as it needs expensive templates for synthesis along with time consuming tedious carbonization process.[37]

Alternatively, using electrospinning; with advantages like, simplicity, scalability, versatility, environmental friendly and low cost fabrication approach, high N-content and highly porous carbon material can be obtained easily.[38] Generally to obtain such material, electrospinning of N-containing polymer as a precursor material with subsequent carbonization process under an inert atmosphere is involved. Using this approach, so far, a wide range of N source polymers (PAN [39], PANi [40,41]and Polyvinyl pyrrolidone, PVP[42]) have been reported for SCs application. However, the carbon product obtained without physical or chemical activation by this approach result limited surface area due to the cylindrical fiber morphology. In order to increase the surface area and porosity of carbon prepared by this method, a post activation process using KOH treatment was followed.[43] It is well known that the activation process could also decrease the N-content yield in carbon materials. In this regard, Young et al. attempted post N-doping using melamine as N-precursor and followed by post heating process, to conceded a high N-content of 9.1 at% with high surface area, which result multiple synthesis strategies.[44] Hence, increases the production cost which isn't beneficial to the commercial application.

We recently reported, the high N-content of arch (8.70 wt%) and hollow (8.22 wt%) shaped nanocarbons with the appreciable surface areas, were prepared without the activation process, whatsoever, for the CO_2 sequestration application.[45] As motivated from our previous study, in this work, we emphasize the notable physio-chemical characteristics of arch and hollow nanocarbons

could also be beneficial to energy storage applications; particularly as electrode materials in SC applications. These materials are developed by a simple co-axial electrospinning approach using a N-source polymer and a sacrificial polymer. Then, followed by non-harmful leaching and non-hazardous carbonization processes. Hence, arch (ACNR) and hollow (HCNR) shaped nanocarbons were acquired. The developed N-doped nanocarbons with a high texture and a N-content characteristic, ACNR, electrode material has delivered an excellent charge storage and charge retention capability.

2. Experimental

To fabricate N-doped ACNR and HCNR nanocarbons a simple co-axial preparation method were followed; using two different polymer materials, PAN (Mw= 150,000 $gmol^{-1}$) act as C, N source precursor of 10 wt% and PVP (Mw= 1,300,000 g mol^{-1}) act as a sacrificial material of 20 wt% in 10 ml of *N*,*N*-dimethylformamide (DMF) at 80 ^{o}C, separately, were used to fabricate electrospun ACNR and HCNR membranes; PAN and PVP polymer solutions were co-axially flowed at different flow rates 1.0 and 0.5 mL hr^{-1} for ACNR, and 0.5 and 0.1 mL hr^{-1} for HCNR fabrication. The obtained electrospun ACNR and HCNR membranes were dipped in hot deionized water at 75 ^{o}C for overnight to leach a hydrophilic polymer, PVP. Finally, the leached membranes were subject to stabilization at 250 ^{o}C for 2 h under air atmosphere and carbonization at 800 ^{o}C for 1h under Argon atmosphere. For comparison, a conventional cylindrical carbon fiber, using a single spinneret electrospinning approach, of 10 wt% PAN electrospun membrane was prepared by following the same pyrolysis protocol as applied in ACNR and HCNR fabrication, and named as CNR.

2.1. Electrochemical Characterizations

All electrochemical measurements were carried at room temperature using Biologic bi-potentiostat VSP-Modular 2 channels. The electrochemical measurements for SC are carried out in both two and three electrodes system configurations under 1M H_2SO_4 electrolyte. In three electrode system, the platinum wire, Ag/AgCl and active material coated glassy carbon (0.0760 cm^2) served as current collector, reference and working electrodes, respectively. For three electrode system measurements, 2.5 mg of active material was dispersed in 150 µl isopropyl alcohol and 2 µl Nafion (5%) using an ultrasonic bath for 30 min and a mass loading of ~0.3mg was kept constant for all the samples. Prior to electrochemical analysis, the electrolyte solution was de-aerated in N_2 for 30 min.

The two electrode systems were made from a homemade symmetric cell setup with Whatman glass fiber (GF) filter paper (70 mm diameter) as a separator material, as depicted in Fig. S1. The working electrode was fabricated by mixing the active material (80%) and polyvinylidene difluoride (20% PVDF) with *N*-methylpyrrolidone (NMP) as a solvent and dried in oven for 70 ^oC overnight, about ~4 mg of active material was coated by this process. The mixture was rolled into a stainless steel current collector (20 µm thickness) and punched into circular discs with a diameter of 1.5 cm (1.766 cm^2 electrode area). The GF separator was impregnated with N_2 saturated electrolyte solution in argon filled glove box (1 bar) and it was placed in between the punched working electrode discs with stainless steel materials as outer terminal connecting leads for both the electrodes, as illustrated in Fig. S1a. The two electrodes symmetric cell was sealed with polyethylene sheet for compactness and to avoid with the atmospheric air contamination.

3. Results and discussion

3.1 Design of Arch and hollow shaped carbon nanostructures

The experimental methodology followed in this work to fabricate N-doped porous HCNR and ACNR is illustrated in Fig.1. The morphological evolution was observed in all the samples during each synthesis step: In step (1) HCNR and ACNR electro-spun fibrous membrane from a co-axial electrospinning process show cylindrical fibrous morphologies with average diameters of 270 and 330 nm, respectively (Fig. S2c-f). However, in step 2, after leaching in hot deionized water observation shows modification in morphologies as shown in Fig. S3a-d. In step (3), carbonization of leached ACNR and HCNR membranes showed the arch and hollow carbon nanostructure with the average diameter of 155 nm and 180 nm, respectively (Fig. 2a-d). Particularly, HCNR samples show a core diameter of 40 to 70nm. Significantly, during the carbonization process, a lower heating rate of 2°C min^{-1} at 250°C for stabilization and a higher heating rate of 5°C min^{-1} at 800°C for carbonization were followed to obtain a high carbon and N content. The morphological evolution in ACNR and HCNR were further asserted by FE-TEM observation as shown in Fig. 2 e, f. Additionally, the comparative sample, CNR displays typical cylindrical rod shaped morphology with an average fiber diameter of 255 nm as shown in Fig. S4a, b and Fig. S4c, d.

3.2 Structural and elemental analysis

To understand the carbon structural defects or ordered/disordered carbon crystal nature due to hetero-atoms, the Raman spectroscopy was carried out for all the samples, as shown Fig. 3. The observed Raman scattering peaks at 1330 and 1575 cm^{-1} correspond to the disordered (sp^3) and ordered (sp^2) carbon domains of D band and G band, respectively. The ratio of D and G band (I_D/I_G) intensities was calculated using a Gaussian fitting method, to understand the structural defects of carbon in each sample. The ratio of D and G bands (I_D/I_G) values found to be 0.97, 1.09 and 1.03

for CNR, HCNR and ACNR samples, respectively. All samples show similar I_D/I_G values near to one which indicates the existence of more structural defects in carbon structure. So the majority of carbon structures of all the samples were turbostatic in nature.

The CHN elemental analysis (EA) and XPS techniques were carried out to measure the detailed elemental composition and the nature of N-species on the surface of all N-doped carbon nanostructured samples. The N content obtained from EA analysis was found to be 9.09, 8.83 and 9.02 (wt%) for CNR, HCNR and ACNR samples, respectively.

The XPS of N-doped carbon nanostructures (CNR, HCNR and ACNR) shows strong signals of carbon, nitrogen and oxygen and the observed peaks were deconvoluted using Gaussian-Lorentz peak fitting. The C1s spectra of all the samples (Fig. 4a) show four distinct peaks, which were deconvoluted and tabulated in Table S1. The dominant peak at C1 (285.1 $\pm$ 0.1 eV) observed for ACNR, HCNR and CNR were assigned to aliphatic carbon (sp^3).[46] The observed C1 peak (284.4 $\pm$ 0.1 eV) of all the samples corresponds to graphitic carbon (sp^2).[46] Also, the peak C3 (285.6$\pm$ 0.2 eV) and C4 (286.5 $\pm$ 0.2 eV) originates from the presence of C-N and C-NHx groups,[47] respectively which proves that N was doped into the carbon framework. The deconvoluted C1s spectra (Table S2) shows majorly amorphous carbon with traces of 12%, 11% and 20% graphitic (sp^2) of CNR, HCNR and ACNR, respectively.

In Fig. 4b, the deconvoluted N 1s spectra of all the samples show two major peaks with binding energy values of 398.3 $\pm$ 0.1 eV (N1) and 401.0 $\pm$ 0.1 eV (N2), which are attributed to pyridinic and quaternary nitrogen groups [48] (Table S1). The N-functionalities in the carbon framework were schematically shown in Fig. 4d. The pyridinic-N (N1), a typical nucleophilic group, on the carbon edge sites possessing a localized electron pair could contribute electrophilic substitution or

elimination reactions;[49] Quaternary-N (N2), replaces a graphitic C atom in a hexagonal ring, improves the charge density of carbon atoms.[50] The peak deconvolution analysis (Table S3) shows that the amount of pyridinic (N1) in the CNR, HCNR and ACNR is found to be 30, 37 and 35%, respectively. In other words, all the sample holds more number of quaternary-N in the carbon framework than the edge sites and thus the energy gap differences between Highest Occupied Molecular Orbital (HOMO) and the Lowest Unoccupied Molecular Orbital (LUMO) is smaller, hence, the conductivity could be enhanced. [50] To correlate this fact, the electrical conductivity of all samples was studied using a four probe measurement and the conductivity values found to be 5.1, 4.2, 4.5 S cm^{-1} for CNR, HCNR and ACNR, respectively. Further, the N-content estimated from the XPS for CNR, HCNR and ACNR samples are 9.78, 8.22 and 8.70 (wt %), respectively, with experimental error of $\pm$ 0.4 % which agrees well with EA results.

The XPS results of O1s spectra for CNR, HCNR and ACNR samples inferred the presences of C=O, C-OH and C-O functional groups (Fig. 4c and Table S1). Such oxygen functional groups are generally basic in nature, which means N-doped ACNR, HCNR and CNR are favorable for the formation of acid-base conjugates when acid electrolyte used than alkaline electrolyte [51]. Therefore, N-doped CNR, HCNR and ACNR samples could be favored as electrode materials in the acid medium electrolyte.

The specific surface area and pore structure of N-doped CNR, HCNR and ACNR were determined by N_2 adsorption-desorption isothermal analysis. Fig. 5a represents isotherms plot of all the samples. Both ACNR and CNR exhibits similar type I isotherms, whereas, HCNR sample shows type I and type IV isotherms. The differences in isotherms are due to different morphology of all the samples and their adsorption ability. The pore size distribution and micro pores information are obtained from Nl-DFT (Fig. 5b) and T-plot method. The BET surface areas of

ACNR, HCNR and CNR are 619, 557 and 484 $m^2 g^{-1}$, respectively. The Nl-DFT total pore volume of ACNR and HCNR and CNR as 0.6589, 0.5681 and 0.4803 cm^3g^{-1}, respectively. Also, to understand the geometry of pore textures the Horvath-Kawazoe method for slit shape pore size was evaluated as pore volume of 0.4675, 0.4063 and 0.3657 cm^3g^{-1} slit shaped pore volume in ACNR, HCNR and CNR, respectively. The micropore surface areas from the t-plot method are 432, 417, and 334 $m^2 g^{-1}$ for ACNR, HCNR, and CNR samples, respectively. All the samples indicate 70-74% micro porosity. Indeed, the differences in the BET surface area of each sample were attributed to the differences in micropore surface areas which result from the morphological effect of each sample during carbonization. It is noted that the samples (ACNR and HCNR) exhibit high surface area, pore volume and micro-pores which could be highly suitable for electro-sorptions in SCs application.

3.3 Electrochemical performance of the N-doped ACNR, HCNR and CNR.

Based on the excellent physicochemical properties, the N-doped ACNR and HCNR are utilized as the electrode materials for SC application. The electrochemical capacitive behavior was first studied in three electrode system under 1M H_2SO_4. Fig. 6a shows the CV curve obtained at 5mV s^{-1} for ACNR, HCNR and CNR, with a specific capacitance value of 406, 346 and 235 Fg^{-1}, respectively. The CV curves resemble a quasi-rectangular shape i.e., the existence of both faradic and non-faradic mechanism for charge storage. The sloped curve observed in the cathodic region was accounted for pseudocapacitance, due to the interaction of protic ion (H_3O^+) on N surface functionalities, pyridinic group.[52]. The following reaction is responsible for the pseudocapacitance mechanism on pyridinc-N carbon nanorods is represented below: [53]

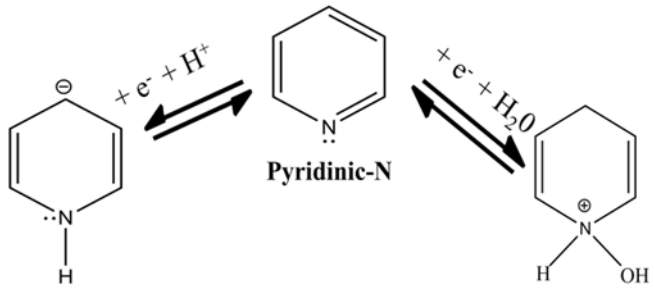

It is noted that, the presence of N-functional groups improves the basicity of carbon material. Hence, enhances the electric double layer adsorption in acidic electrolyte medium, 1 M H_2SO_4. A high capacitance of 417 F g^{-1} was obtained for ACNR sample at a low scan rate of 2mV s^{-1}, as shown in Fig. 6a. To understand the rate capability of each material, different scan rates (2, 10, 20 50 and 100 mV s^{-1}) were employed for all samples as shown in Fig. S5 a-c and the obtained results were plotted in Fig. 6b.

The charge-discharge profiles of all samples show near symmetric shape suggesting a good reversibility. Fig. 6c shows the charge-discharge profiles performed at 0.5 A g^{-1} for ACNR, HCNR and CNR samples, which exhibits the C_{sp} of 421, 371 and 227 F g^{-1}, respectively. Further, the charge-discharge studies were carried out with various current densities (1 to 20 A g^{-1}) for all the samples, as shown in Fig. S5 (d-f) and S6 (a-c). Similar to CV studies ACNR sample shows outstanding performance with a maximum C_{sp} of 432 F g^{-1} at a low current density (0.25 A g^{-1}) and the specific capacitance still be maintained to 345 F g^{-1} at a high current density of 5 A g^{-1} in comparison to CNR and HCNR samples, as shown in Fig. 6d. Such high performance of ACNR in comparison to other samples (HCNR and CNR) was attributed to a high surface area with a high micro- pore texture and accessible N-functionalities content; such features are responsible for ion transport and superior rate performance. However, the performance obtained from the three-electrode systems cannot be used for practical application, but gives a clear understanding of our material electrochemical behaviors as a single electrode.

In SCs application, generally, the two electrode system is used for real understanding of electrode material evaluations by means of electrochemical performance, in comparison to three electrode system based material evaluations.[54] Also, the C_{sp} obtained by two electrode system gives a lower value than three electrode system but with a real material performance owing to fact that in three electrode cell, the whole potential is applied to a single electrode, whereas in two electrode cell the applied potential is divided equally in two electrodes which makes huge difference in capacitance value. Hence, the two electrode system with the symmetric electrode configuration was studied for ACNR, HCNR and CNR electrode materials in 1M H_2SO_4. Fig. 7a shows CV curves obtained at 5mV s^{-1} for ACNR (224 F g^{-1}), HCNR (209 F g^{-1}) and CNR (167 F g^{-1}) displays a rectangular shaped with a small electrolyte diffusion limit. However, in contrast to three electrode system the CVs show more ideal EDLC behavior, despite of N and O functionalities existence, which is in consistence with previous reports.[55–58] Further, the CV at different scan rates (2, 10, 20, 50 and 100 mV s^{-1}) was performed for all the samples as shown in Fig. S7 (a-c) and the evaluated results displayed in Fig. 7b. The maximum C_{sp} of 230, 212 and 170 F g^{-1} at 0.1 A g^{-1} was obtained for ACNR, HCNR and CNR samples, respectively. Particularly, ACNR sample at high scan rate (100 mV s^{-1}) shows a capacitance value of 190 F g^{-1}, which indicates an excellent rate capability of 82% in comparison to a C_{sp} value obtained at 2 mV s^{-1} scan rate. Fig. 7c, shows galvanostatic charge-discharge measurements at a current density 0.2 A g^{-1} for all samples with the ideal symmetric behavior, which validates the CV ideal rectangular behavior. The maximum C_{sp} of 232, 220 and 152 F g^{-1} at a current density of 0.1 A g^{-1} for ACNR, HCNR and CNR was obtained, respectively. Fig. 7d, S7d-f and S8a-c depicts the C_{sp} as a function of different current densities (0.1 to 20 g^{-1}). Also, to understand the rate performance of each samples the IR drop potential was evaluated from the discharge curve, which shows a negligible IR drop up to 5 A/g.

However, with further increasing the charge-discharge rates the ACNR, HCNR and CNR materials show the maximum IR drop potentials of 0.07, 0.15 and 0.2V, respectively, as shown in Fig. S9. Further, equivalent series resistance (ESR) values were evaluated using the slope of linear correlation between the IR drop voltage and discharge current densities of ACNR, HCNR and CNR as 3.17, 6.17 and 8.28 mΩ, respectively, as shown in Fig. S9. Notably, the ACNR material exhibit low IR drop and ESR value indicates good rate performance.

Further, the low C_{sp} of CNR than ACNR and HCNR could be attributed to the morphological restrictive over the electrolyte accessibility and limited redox mechanism of pyridinic N-species content in CNR as explained in XPS inferences. Also, the C_{sp} values obtained from two electrode system are lower than those evaluated from three electrode system, which is reasonable due to the electrode configuration differences in both the case. However, the C_{sp} values obtained from the two electrode system are comparable with previous reports for N-doped carbon materials performed under acid medium, as listed in Table S4. The comparison of C_{sp} with various N-doped carbon materials clearly show that the comparable or higher C_{sp} values are obtained for N-doped HCNR and ACNR samples from this work.

To realize the practical application of developed electrode materials, the long term cycle stability test for ACNR, HCNR and CNR samples were evaluated by galvanostatic charge-discharge at 1 A g^{-1} for 5000 cycles, as shown in Fig. 8a. ACNR and HCNR samples show an increasing C_{sp} at initial cycles are presumed to be electrolyte ion diffusion in highly micro porous electrode textures and also the contribution of oxygen functional groups. All samples show excellent capacitance retention of ~98%, which indicate a high degree of reversibility. To understand the material stability after 5000 cycles, all the cycled cells were dismantled and their corresponding electrodes are subjected to morphology analysis as shown in Fig. S10 (a-f). The

results show no change in surface texture of ACNR, HCNR and CNR electrodes which validate the long term cycle stability test. The Ragone plot (energy density, E vs. power density, P) of symmetrically configured ACNR, HCNR and CNR systems displayed the E (Wh kg^{-1}) of 8.4, 7.5 and 5.0 Wh kg^{-1}, respectively, as shown in Fig. 8b. The P (W kg^{-1}) calcualted for ACNR, HCNR and CNR samples as 1.2, 1.0 and 0.9 kW kg^{-1}, respectively. These results suggest that ACNR and HCNR electrode material can deliver high and comparable E (Wh kg^{-1}) in comparison to previously reported (Table S4) N-doped and N-free carbon materials evaluated in acid medium.

The EIS measurements were carried out for ACNR, HCNR and CNR samples in two electrode system to further understand the electrochemical performance characteristics. The measurements were carried out with an open circuit voltage in the frequency range from 200 kHz to 10 mHz with a perturbation potential of 10 mV AC amplitude. Fig. 8c shows the Nyquist plots observed of all samples which are fitted using Z_{view} software based on an equivalent circuit model, consisting of internal resistance (R_1), charge transfer resistance (R_{CT}), constant phase element (CPE) and Warbug impedance (Wo). The EIS result shows that ACNR samples exhibit smaller R_{CT} values 0.34 Ω as compared to HCNR and CNR samples 0.53, 1.78 Ω for ACNR, HCNR and CNR samples respectively. Such low R_{CT} values in ACNR and HCNR are attributed to fast electrolyte ion-diffusions in electrode and electrolyte interface.

Based on the comparison, N-doped ACNR and HCNR samples were fabricated using a cost effective approach and these carbon materials delivered a comparable and higher E than any other reported N-doped carbon materials, which was performed in H_2SO_4 medium i.e., similar to our electrochemical analysis conditions. Competitively, as listed in Table S4, polyaniline composites[59] delivered four times higher E, 27.4 Wh kg^{-1} than the E values of ACNR and HCNR nanocarbons. However, considering the SC key performances, ACNR and HCNR devices exhibit the low IR

drop potential at high charge/discharge rate, low ESR values and prolonged cycle life time which outperformed the polyaniline composites.

Based on the above electrochemical experimental demonstration, the superior performance of the symmetrical ACNR and HCNR SCs can be attributed to the following aspects: (1) High surface area of ACNR and HCNR with highly doped-N plays an excellent key for SC behavior. In the case of CNR, despite of having high N-content than ACNR and ACNR but its performance was limited by inaccessible active surface area as illustrated in Fig. 9, (2) Good electrode and electrolyte interface favours for fast ionic diffusion with low charge transfer resistance, (3) Slit or narrow pore sized geometry promotes short ionic diffusion length, as illustrated in Fig. 9 for better understanding. These interesting results could be highly suitable for high performance SCs in practical applications.

4. Conclusions

In this work, we have developed two unconventional N-doped nano carbons of different morphologies, ACNR and HCNR, using a simple co-axial electrospinning technique. Amongst different nano carbons, the physicochemical studies of ACNR have a high surface area of 619 m^2g^{-1}, a pore volume of 0.4803 cm^3g^{-1}, a high N-content of 9.02 wt%. Such desirable properties of ACNR were utilized in SCs applications using full cell symmetric configuration. For the comparison HCNR and CNR nano carbons were also studied. The electrochemical studies reveal that ACNR possesses excellent supercapacitor performances such as high C_{sp} (238 F g^{-1}), low IR drop potential (0.07 V) and ESR (3.17 mΩ) at a high current density of 20 A g^{-1} as compared with HCNR and CNR nano carbons, which are solely attributed to the textural properties of ACNR nano carbon. Moreover, ACNR material exhibits maximum E (8.4 Wh kg^{-1}) and good long term 5000 cycle stability with charge retention of 98 % at 1 A g^{-1}. We believe that the outstanding

results would pave the way of exploring ACNR and HCNR unique N-doped nano carbon structures in applications related to H_2 adsorption, electro-catalyst for CO_2 reduction, energy storage, separation, and medicine.

Acknowledgements

This work was supported by the DGIST R&D Program of the Ministry of Education, Science and Technology of Korea (15-BD-01) and also partly by the DGIST MIREBraiN program.

Electronic Supplementary Information (ESI)

Supplementary data associated with this article can be found in the online version.

References

1. Y. Gogotsi, A. Nikitin, H. Ye, W. Zhou, J. E. Fischer, B. Yi, H. C. Foley, and M. W. Barsoum, *Nat. Mater.*, 2003, **2**, 591–4.

2. Z.-S. Wu, Y. Sun, Y.-Z. Tan, S. Yang, X. Feng, and K. Müllen, *J. Am. Chem. Soc.*, 2012, **134**, 19532–5.

3. R. K. Motkuri, H. V. R. Annapureddy, M. Vijaykumar, H. T. Schaef, P. F. Martin, B. P. McGrail, L. X. Dang, R. Krishna, and P. K. Thallapally, *Nat. Commun.*, 2014, **5**, 4368.

4. H. Wang, Q. Gao, and J. Hu, *J. Am. Chem. Soc.*, 2009, **131**, 7016–22.

5. J. Wang, H. Zhong, Y. Qin, and X. Zhang, *Angew. Chem. Int. Ed. Engl.*, 2013, **52**, 5248–53.

6. Y. Liang, Y. Li, H. Wang, and H. Dai, *J. Am. Chem. Soc.*, 2013, **135**, 2013–36.

7. Y. Li, T. Ben, B. Zhang, Y. Fu, and S. Qiu, *Sci. Rep.*, 2013, **3**, 2420.

8. X. H. Xia, D. L. Chao, Y. Q. Zhang, Z. X. Shen, and H. J. Fan, *Nano Today*, 2015, **9**, 785–807.

9. X. Xia, D. Chao, Z. Fan, C. Guan, X. Cao, H. Zhang, and H. J. Fan, *Nano Lett.*, 2014, **14**, 1651–1658.

10. R. E. Morris and P. S. Wheatley, *Angew. Chem. Int. Ed. Engl.*, 2008, **47**, 4966–81.

11. Q. Yang, W. Xu, A. Tomita, and T. Kyotani, *J. Am. Chem. Soc.*, 2005, **127**, 8956–7.

12. D.-W. Wang, F. Li, Z.-G. Chen, G. Q. Lu, and H.-M. Cheng, *Chem. Mater.*, 2008, **20**, 7195–7200.

13. R. Babarao, S. Dai, and D. Jiang, *J. Phys. Chem. C*, 2012, **116**, 7106–7110.

14. Y. J. Oh, J. J. Yoo, Y. Il Kim, J. K. Yoon, H. N. Yoon, J.-H. Kim, and S. Bin Park, *Electrochim. Acta*, 2014, **116**, 118–128.

15. E. Cruz-Silva, F. López-Urías, E. Muñoz-Sandoval, B. G. Sumpter, H. Terrones, J. Charlier, V. Meunier, and M. Terrones, *ACS Nano*, 2009, **3**, 1913–21.

16. L. Zhang, J. Niu, M. Li, and Z. Xia, *J. Phys. Chem. C*, 2014, **118**, 3545–3553.

17. Y. Guo, Z. Shi, M. Chen, and C. Wang, *J. Power Sources*, 2014, **252**, 235–243.

18. Z. Yang, Z. Yao, G. Li, G. Fang, H. Nie, Z. Liu, X. Zhou, X. Chen, and S. Huang, *ACS Nano*, 2012, **6**, 205–11.

19. J. Wei, D. Zhou, Z. Sun, Y. Deng, Y. Xia, and D. Zhao, *Adv. Funct. Mater.*, 2013, **23**, 2322–2328.

20. J. Sanetuntikul and S. Shanmugam, *Electrochim. Acta*, 2014, **119**, 92–98.

21. S. L. Candelaria, B. B. Garcia, D. Liu, and G. Cao, *J. Mater. Chem.*, 2012, **22**, 9884.

22. X. Xia, Y. Zhang, Z. Fan, D. Chao, Q. Xiong, J. Tu, H. Zhang, and H. J. Fan, *Adv. Energy Mater.*, 2015, **5**, 1401709.

23. J. R. Pels, F. Kapteijn, J. A. Moulijn, Q. Zhu, and K. M. Thomas, *Carbon,* 1995, **33**, 1641–1653.

24. X. Xia, D. Chao, C. F. Ng, J. Lin, Z. Fan, H. Zhang, Z. X. Shen, and H. J. Fan, *Mater. Horiz.*, 2015, **2**, 237–244.

25. L.-F. Chen, X.-D. Zhang, H.-W. Liang, M. Kong, Q.-F. Guan, P. Chen, Z.-Y. Wu, and S.-H. Yu, *ACS Nano*, 2012, **6**, 7092–102.

26. D. Hulicova-Jurcakova, M. Kodama, S. Shiraishi, H. Hatori, Z. H. Zhu, and G. Q. Lu, *Adv. Funct. Mater.*, 2009, **19**, 1800–1809.

27. D. Hulicova-Jurcakova, M. Seredych, G. Q. Lu, and T. J. Bandosz, *Adv. Funct. Mater.*, 2009, **19**, 438–447.

28. C. Liang, Z. Li, and S. Dai, *Angew. Chem. Int. Ed. Engl.*, 2008, **47**, 3696–717.

29. B.-H. Han, W. Zhou, and A. Sayari, *J. Am. Chem. Soc.*, 2003, **125**, 3444–5.

30. X. Xu, B. Dong, S. Ding, C. Xiao, and D. Yu, *J. Mater. Chem. A*, 2014, **2**, 13069.

31. X. Xu, H. Tan, K. Xi, S. Ding, D. Yu, S. Cheng, G. Yang, X. Peng, A. Fakeeh, and R. V. Kumar, *Carbon*, 2014, **84**, 491–499.

32. D. Guo, J. Mi, G. Hao, W. Dong, G. Xiong, W. Li, and A.-H. Lu, *Energy Environ. Sci.*, 2013, **6**, 652.

33. D. Hulicova, M. Kodama, and H. Hatori, *Chem. Mater.*, 2006, **18**, 2318–2326.

34. S. Shrestha and W. E. Mustain, *J. Electrochem. Soc.*, 2010, **157**, B1665.

35. L. Li, E. Liu, J. Li, Y. Yang, H. Shen, Z. Huang, X. Xiang, and W. Li, *J. Power Sources*, 2010, **195**, 1516–1521.

36. M. Zhong, E. K. Kim, J. P. McGann, S.-E. Chun, J. F. Whitacre, M. Jaroniec, K. Matyjaszewski, and T. Kowalewski, *J. Am. Chem. Soc.*, 2012, **134**, 14846–57.

37. L. Hao, X. Li, and L. Zhi, *Adv. Mater.*, 2013, **25**, 3899–904.

38. A. Greiner and J. H. Wendorff, *Angew. Chem. Int. Ed. Engl.*, 2007, **46**, 5670–703.

39. E. Ra, E. Raymundo-Piñero, Y. Lee, and F. Béguin, *Carbon N. Y.*, 2009, **47**, 2984–2992.

40. Y. Cao, L. Xiao, M. L. Sushko, W. Wang, B. Schwenzer, J. Xiao, Z. Nie, L. V. Saraf, Z. Yang, and J. Liu, *Nano Lett.*, 2012, **12**, 3783–3787.

41. S. Chaudhari, Y. Sharma, P. S. Archana, R. Jose, S. Ramakrishna, S. Mhaisalkar, and M. Srinivasan, *J. Appl. Polym. Sci.*, 2013, **129**, 1660–1668.

42. E. Lee, T. Lee, and B. Kim, *J. Power Sources*, 2014, **255**, 335–340.

43. J. Wang and S. Kaskel, *J. Mater. Chem.*, 2012, **22**, 23710.

44. Y. S. Yun, C. Im, H. H. Park, I. Hwang, Y. Tak, and H.-J. Jin, *J. Power Sources*, 2013, **234**, 285–291.

45. P. Ramakrishnan and S. Shanmugam, *RSC Adv.*, 2014, **4**, 59633–59636.

46. S. Kaciulis, *Surf. Interface Anal.*, 2012, **44**, 1155–1161.

47. X. He, F. Zhang, R. Wang, and W. Liu, *Carbon*, 2007, **45**, 2559–2563.

48. S. R. Kelemen, M. L. Gorbaty, and P. J. Kwiatek, *Energy & Fuels*, 1994, **8**, 896–906.

49. C.-C. Hwang, J. J. Tour, C. Kittrell, L. Espinal, L. B. Alemany, and J. M. Tour, *Nat. Commun.*, 2014, **5**, 3961.

50. G. Lota, K. Fic, and E. Frackowiak, *Energy Environ. Sci.*, 2011, **4**, 1592.

51. Y. J. Oh, J. J. Yoo, Y. Il Kim, J. K. Yoon, H. N. Yoon, J. Kim, and S. Bin Park, *Electrochim. Acta*, 2014, **116**, 118–128.

52. P. Ramakrishnan and S. Shanmugam, *Electrochim. Acta*, 2014, **125**, 232–240.

53. U. B. Nasini, V. G. Bairi, S. K. Ramasahayam, S. E. Bourdo, T. Viswanathan, and A. U. Shaikh, *J. Power Sources*, 2014, **250**, 257–265.

54. M. D. Stoller and R. S. Ruoff, *Energy Environ. Sci.*, 2010, **3**, 1294.

55. L. Qie, W. Chen, H. Xu, X. Xiong, Y. Jiang, F. Zou, X. Hu, Y. Xin, Z. Zhang, and Y. Huang, *Energy Environ. Sci.*, 2013, **6**, 2497.

56. Z.-S. Wu, A. Winter, L. Chen, Y. Sun, A. Turchanin, X. Feng, and K. Müllen, *Adv. Mater.*, 2012, **24**, 5130–5.

57. Z. Wen, X. Wang, S. Mao, Z. Bo, H. Kim, S. Cui, G. Lu, X. Feng, and J. Chen, *Adv. Mater.*, 2012, **24**, 5610–6.

58. Z. Li, L. Zhang, B. S. Amirkhiz, X. Tan, Z. Xu, H. Wang, B. C. Olsen, C. M. B. Holt, and D. Mitlin, *Adv. Energy Mater.*, 2012, **2**, 431–437.

59. Z. Lei, X. Sun, H. Wang, Z. Liu, and X. S. Zhao, *ACS Appl. Mater. Interfaces*, 2013, **5**, 7501–8.

Figure captions

Fig. 1. Schematic representation of HCNR and ACNR samples synthesis.

Fig. 2. HCNR sample FE-SEM (a, b) and FE-TEM (e) images; and ACNR sample FE-SEM (c, d) and FE-TEM (f) images.

Fig. 3. Raman spectra of ACNR, HCNR, and CNR samples.

Fig. 4. High resolution XPS spectra: C1s (a), N 1s (b) and O1s(c) for all samples; (d) schematic illustration of nitrogen functional groups for observed N1 s spectra.

Fig. 5. (a) N2 adsorption-desorption isotherms and (b) Nl-DFT pore size distribution of ACNR, HCNR and CNR respectively.

Fig. 6. The three electrode cell based electrochemical performance of all samples in 1 M H_2SO_4: (a) CVs at a 5mV s^{-1} scan rate, (b) Effect of scan rates on C_{sp}, (c) Galvanostatic charge-discharge profiles at a 0.5 A g^{-1} current density and (d) Effect of current densities on C_{sp}

Fig. 7. The symmetric two electrode cell electrochemical performance of all samples in 1 M H_2SO_4: (a) CV curves at a 5mV s^{-1} scan rate, (d) Effect of scan rates on C_{sp}, (c) Galvanostatic charge-discharge profiles at a 0.2 A g^{-1} current density of all samples and (d) Effect of current densities on C_{sp}.

Fig. 8. (a) Long term cycle stability test at a current density of 1 A g^{-1}; (b) Ragone plot (Energy density, E vs. Power density, P); (c) Nyquist impedance plot and inset shows the magnified view at high frequency for all samples, respectively.

Fig. 9. Pictorial representation of electro-sorption of hydronium ions (H_3O^+) on CNR, HCNR and ACNR samples, the surface of N-doped nanocarbons are considered negative potential.

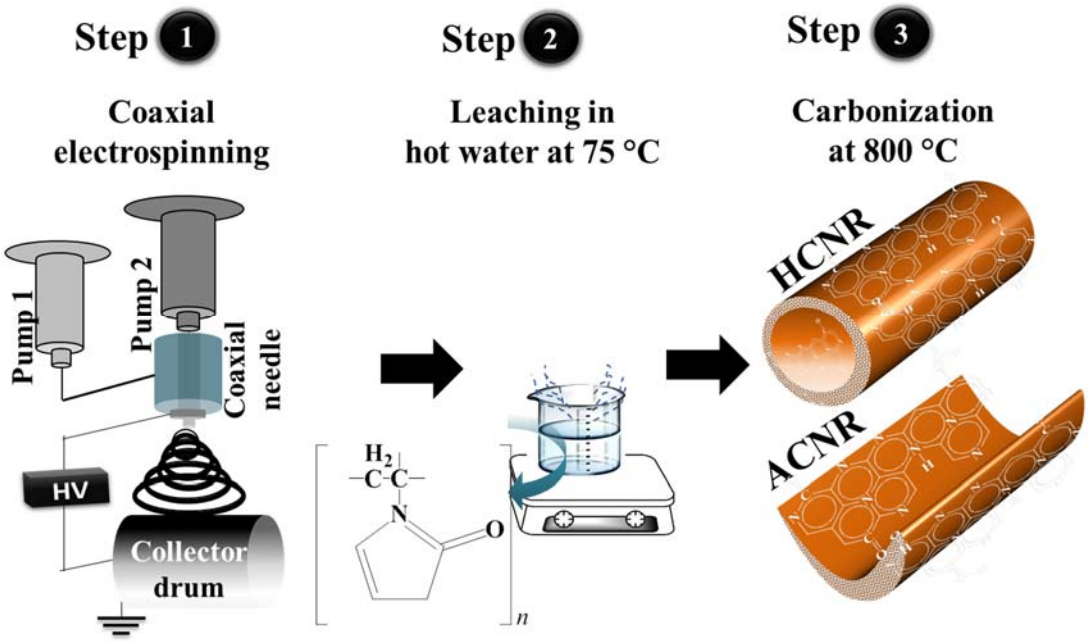

Fig. 1. Schematic representation of HCNR and ACNR samples synthesis.

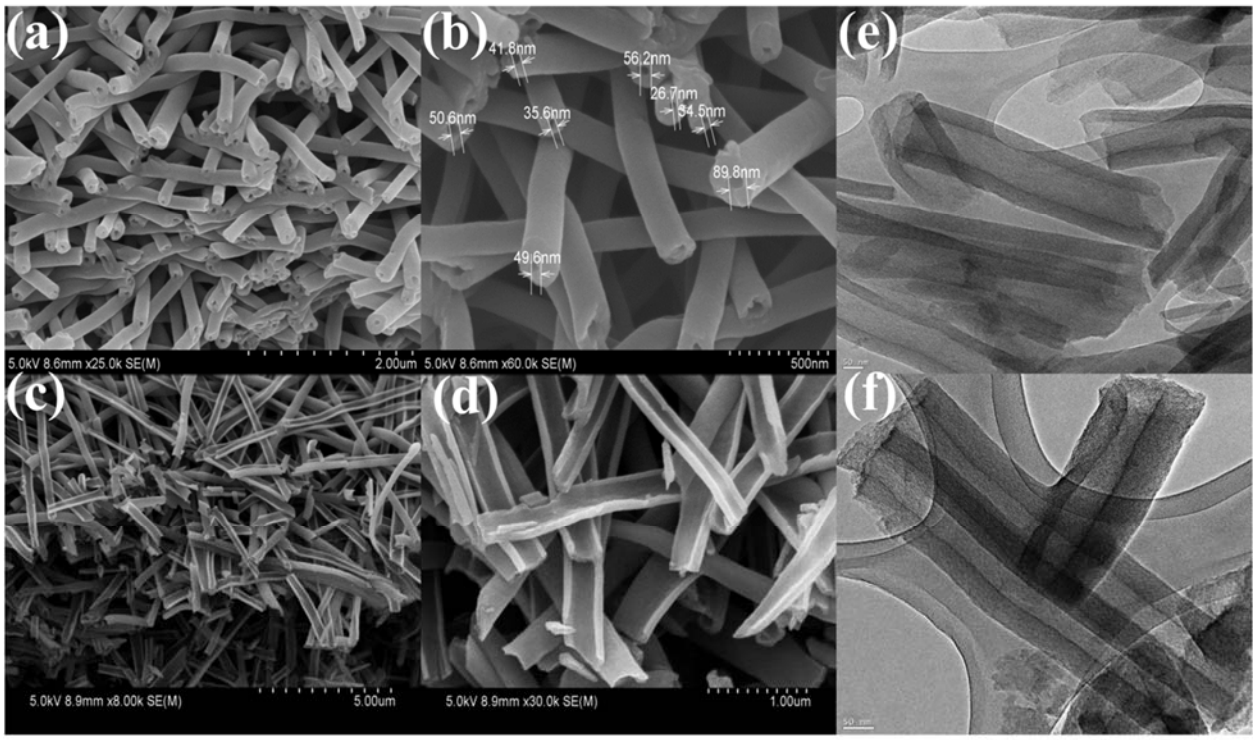

Fig. 2. HCNR sample FE-SEM (a, b) and FE-TEM (e) images; and ACNR sample FE-SEM (c, d) and FE-TEM (f) images.

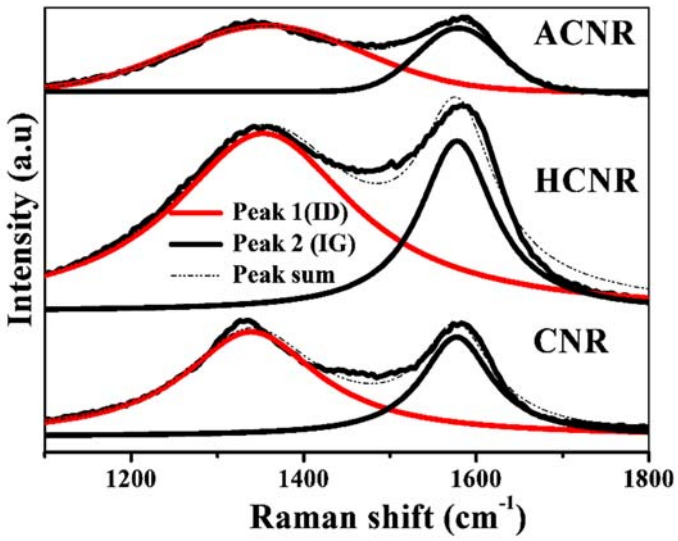

Fig. 3. Raman spectra of ACNR, HCNR, and CNR samples.

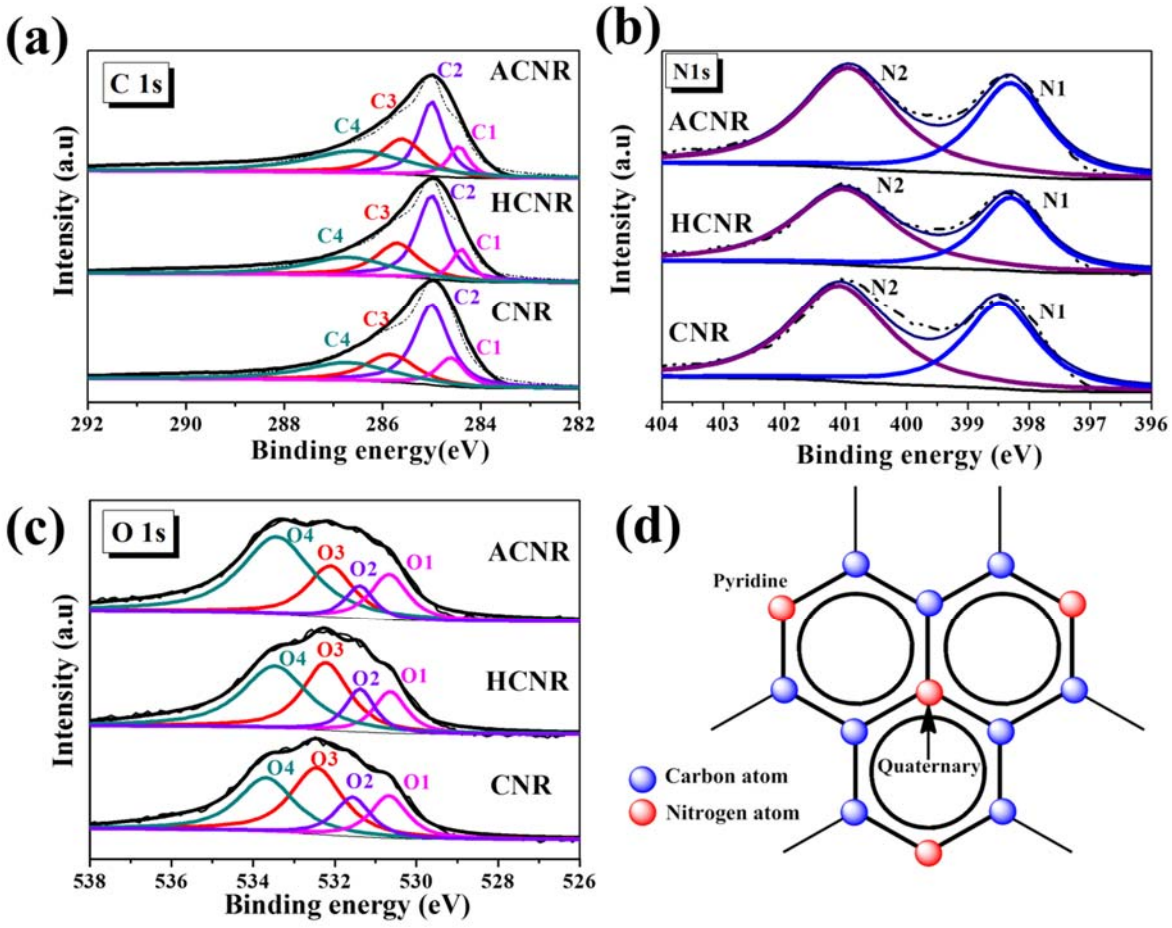

Fig. 4. High resolution XPS spectra: C1s (a), N 1s (b) and O1s(c) for all samples; (d) schematic illustration of nitrogen functional groups for observed N1 s spectra.

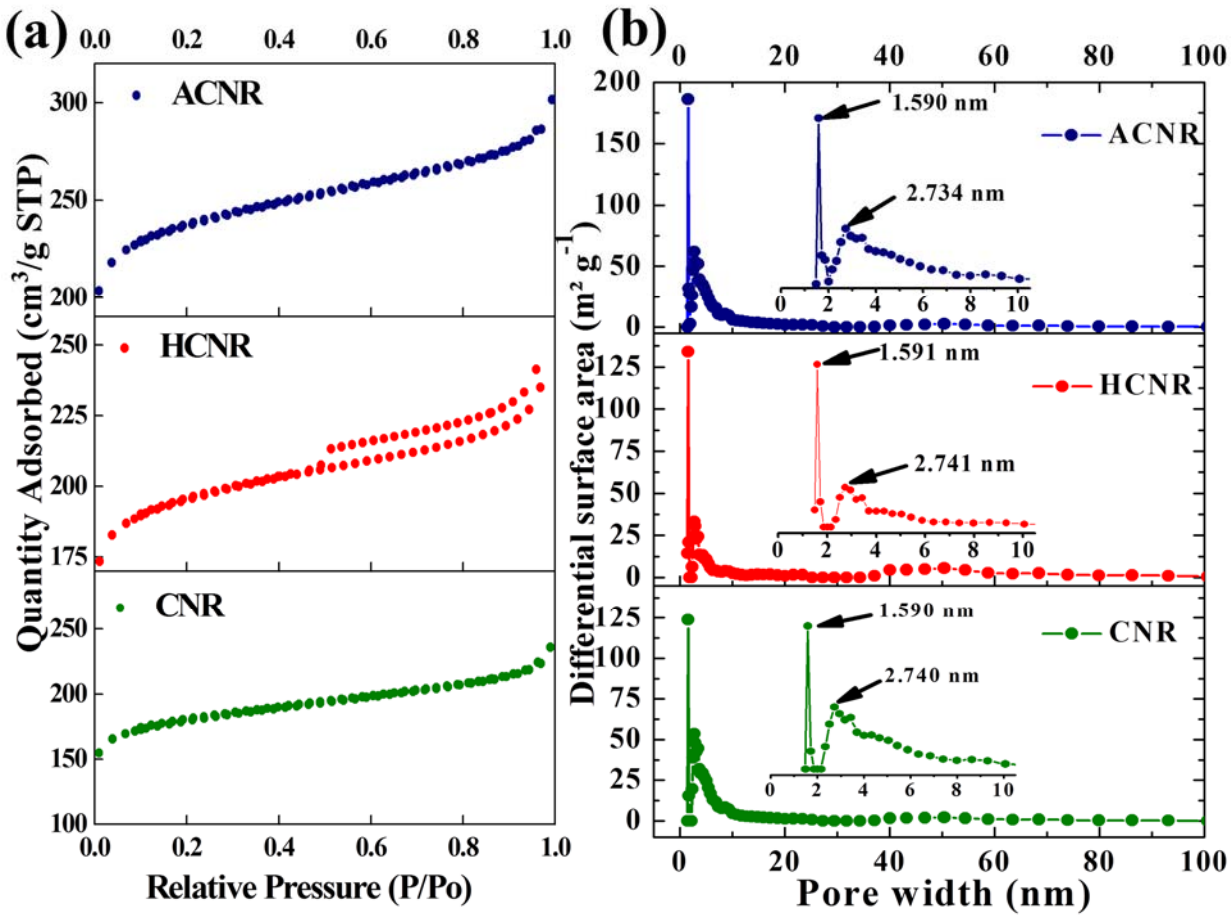

Fig. 5. (a) N_2 adsorption-desorption isotherms and (b) Nl-DFT pore size distribution of ACNR, HCNR and CNR respectively.

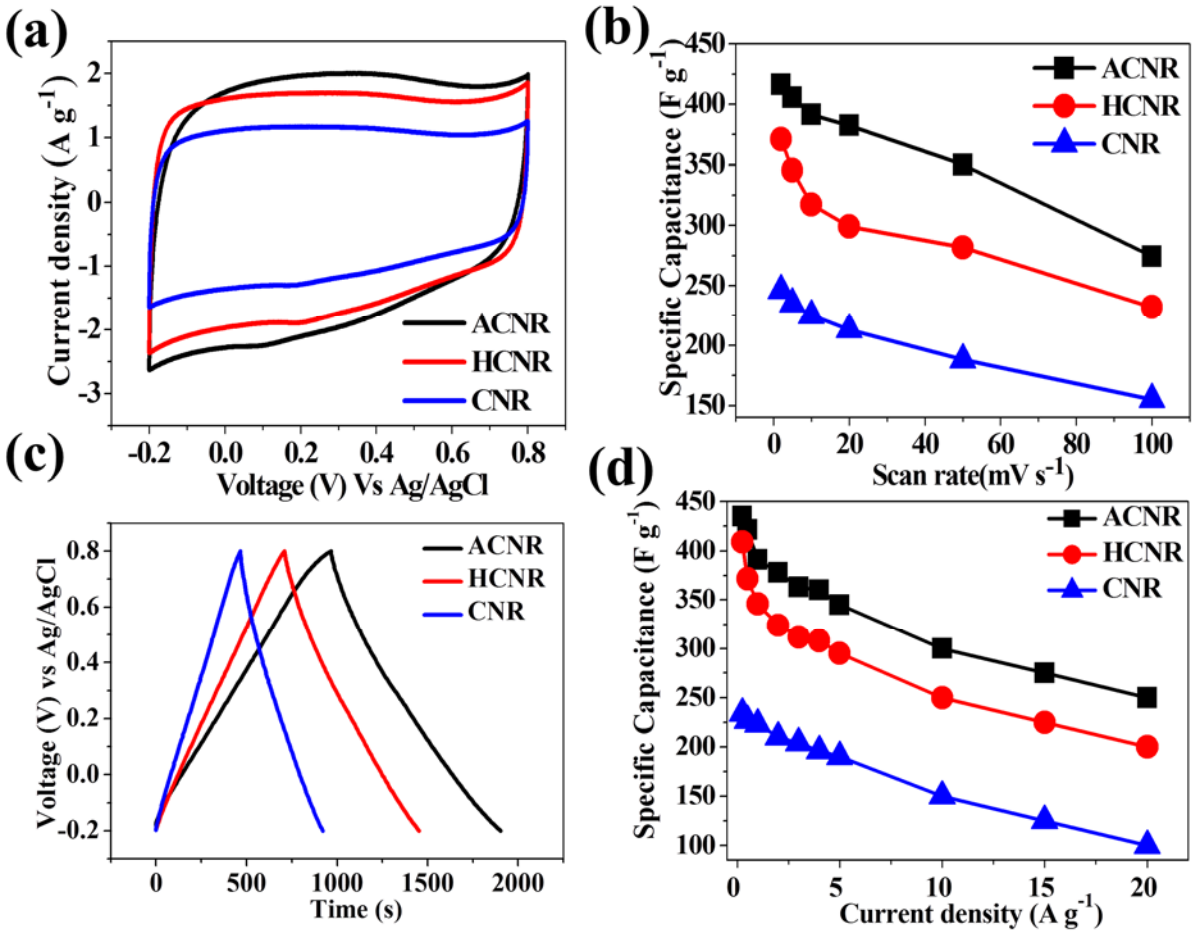

Fig. 6. The three electrode cell based electrochemical performance of all samples in 1 M H_2SO_4: (a) CVs at a 5mV s^{-1} scan rate, (b) Effect of scan rates on C_{sp}, (c) Galvanostatic charge-discharge profiles at a 0.5 A g^{-1} current density and (d) Effect of current densities on C_{sp}

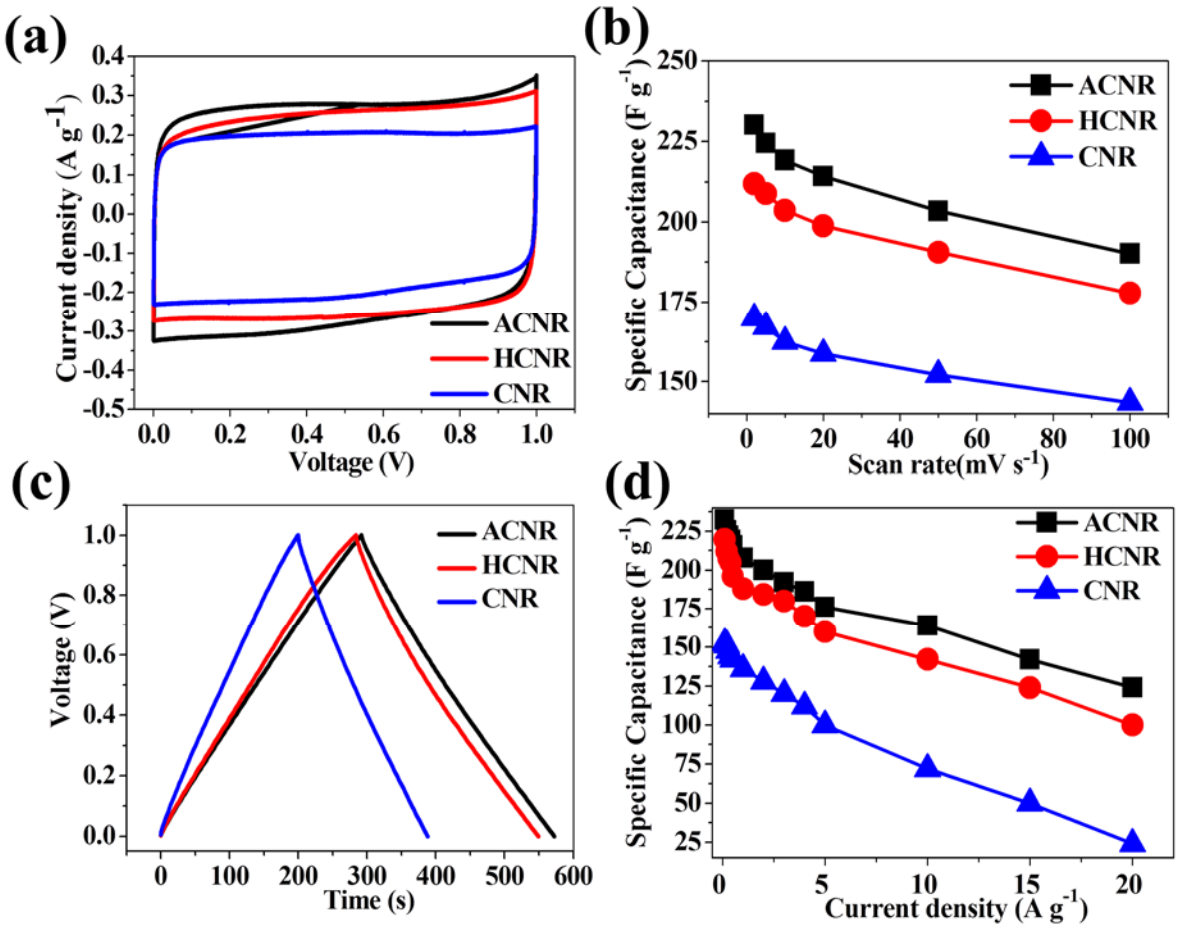

Fig. 7. The symmetric two electrode cell electrochemical performance of all samples in 1 M H_2SO_4: (a) CV curves at a 5mV s^{-1} scan rate, (d) Effect of scan rates on C_{sp}, (c) Galvanostatic charge-discharge profiles at a 0.2 A g^{-1} current density of all samples and (d) Effect of current densities on C_{sp}.

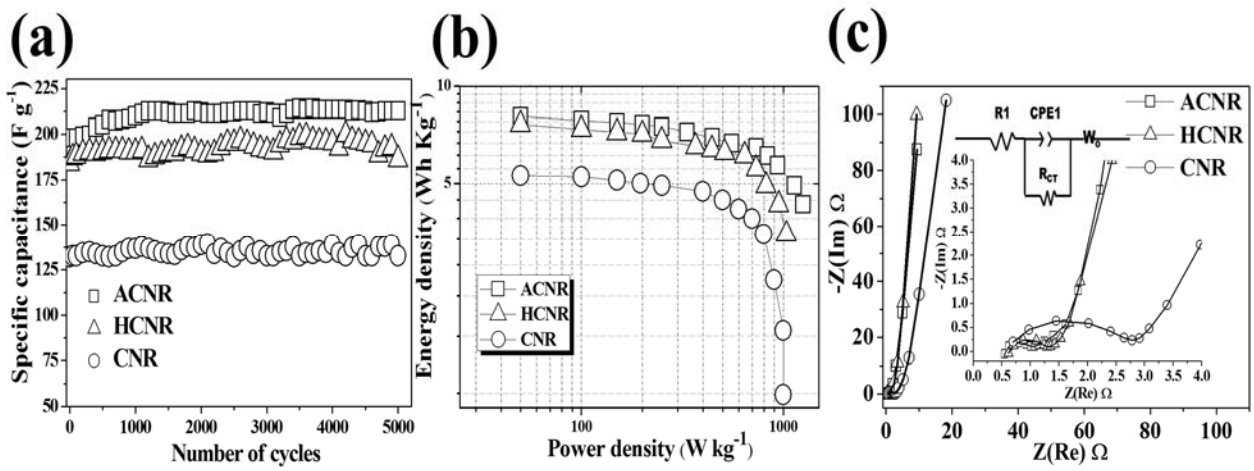

Fig. 8. (a) Long term cycle stability test at a current density of 1 A g^{-1}; (b) Ragone plot (Energy density, E vs. Power density, P); (c) Nyquist impedance plot and inset shows the magnified view at high frequency for all samples, respectively.

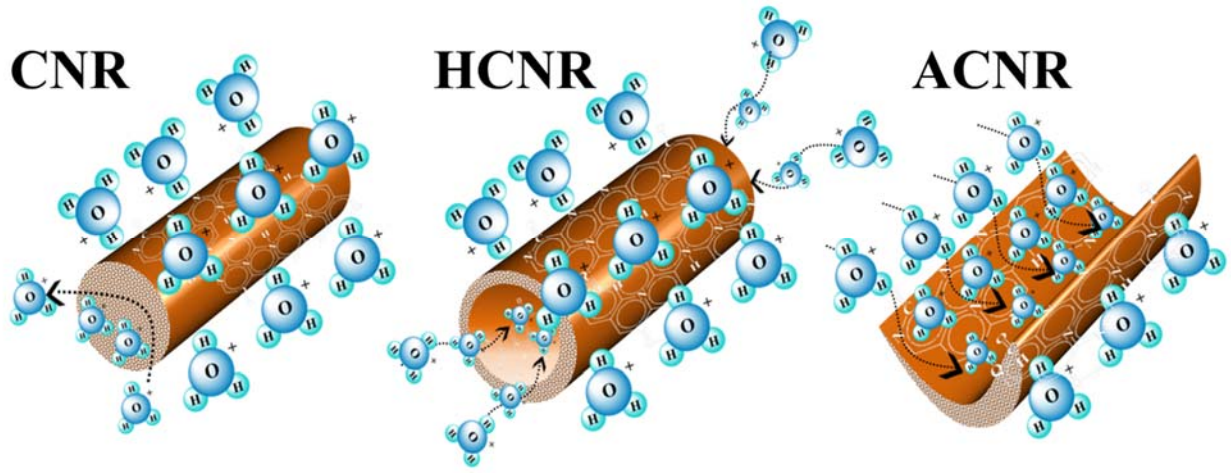

Fig. 9. Pictorial representation of electro-sorption of hydronium ions (H_3O^+) on CNR, HCNR and ACNR samples, the surface of N-doped nanocarbons are considered negative potential.

Graphical abstract

The unique three dimensional hierarchical nitrogen doped nanocarbons prepared using simple approach, exhibits excellent supercapacitor performance in all the aspects.